


Cite this: *RSC Adv.*, 2024, **14**, 21635

Hydrophilicity and surface charge modulation of $Ti_3C_2T_x$ MXene based membranes for water desalination†

Laxmi Pandey,^a Wentao Liang,^a Armin VahidMohammadi,^d Teng Zhang,^d Yury Gogotsi^d and Meni Wanunu  ^{abc}

Lamellar membranes obtained by stacking 2D layers possess ample transport pathways due to their intricate network of interlayer gaps. This makes them suitable for molecular separation applications. However, controlling the surface chemistry of the nanochannels within the membrane to tune the desired transport properties of water and ions is challenging. $Ti_3C_2T_x$ has been considered for water desalination because of its hydrophilic surface and negative surface charge. Most of the studies of $Ti_3C_2T_x$ membranes have presented promising salt rejection values in forward osmosis mode, which is less practical for water purification. Here, we investigate two types of reverse osmosis MXene-based lamellar membranes consisting of $Ti_3C_2T_x$ nanosheets hybridized with (i) WS_2 nanosheets and (ii) polyvinyl phosphonic acid (PVPA). When hydrophilic and flexible $Ti_3C_2T_x$ nanosheets are interleaved with softer and more hydrophobic WS_2 nanosheets in 2:1 mass ratio, nano capillaries with Janus chemistry are created with comparable rejection to bare $Ti_3C_2T_x$ membrane and threefold higher permeance values. Further, we find that decorating $Ti_3C_2T_x$ nanosheets with anionic polymers improves salt rejection. Our $Ti_3C_2T_x$ /PVPA composite membranes reject ~97% of divalent ions and ~80% of monovalent ions with ~0.2 $Lm^{-2} h^{-1} bar^{-1}$ of water permeance when tested with brackish water, and exhibit significantly improved chlorine resistance and cost benefits over the commercial Toray membranes.

Received 10th April 2024

Accepted 29th June 2024

DOI: 10.1039/d4ra02678k

rsc.li/rsc-advances

1. Introduction

Meeting the increasing demand for water for drinking and irrigation is an increasingly important challenge in water security that requires new exploration of new materials and device configurations.¹ One approach involves using advanced two-dimensional (2D) materials with a very large surface-to-volume ratio, as scalable production of these materials is now possible.^{2–4} Membrane laminates prepared from 2D materials consist of numerous interconnected interlayer pathways, which can be tuned to allow a particular type of molecule or ion to pass through them, depending on the size,⁵ charge,⁵ and other characteristics.⁶ Among the 2D materials, graphene oxide (GO) is most studied for nanofiltration and water desalination as GO nanosheets consist of the unoxidized hydrophobic region, which allows ultrafast water transport⁷ as well as the

hydrophilic region, which consists of different functional groups that act as spacers.⁷ A challenge with GO membranes is that interactions of water molecules with the oxygenated functional groups (especially $-COOH$) lead to uncontrolled swelling.⁸ Some attempts, such as physical confinement,⁹ cross-linking¹⁰ and reduction of GO nanosheets^{5,11,12} have addressed the swelling problem in part, but these solutions are not amenable to pressure-driven water desalination.^{5,10} Some studies have shown promising results utilizing membranes made from transition metal dichalcogenides (MoS_2 , WS_2) by controlling their wetting state¹³ and introducing spacers with covalent^{13–15} and non-covalent¹⁶ functionalization as the membrane is water-impermeable in its dry state without functionalization.^{13,14,17} MXenes, a broad class of 2D materials consisting of carbide or nitride layers terminated with surface functional groups,¹⁸ have also been explored for various applications such as energy storage,^{19,20} catalysis,²¹ biomolecule sensing²² and membrane separation.^{23–26} $Ti_3C_2T_x$, where T represents surface terminations such as O, OH, F, and x represents the fraction of surface groups, is the first introduced and most studied MXene.²⁷ Most studies on $Ti_3C_2T_x$ membranes have shown promising ion sieving properties, but only in forward osmosis mode.^{23,24,26} Some studies have used pressurized systems and either observed water permeance only^{25,28} or salt rejection for low salt concentrations.²⁹ To

^aDepartment of Physics, Northeastern University, Boston, MA, 02115, USA

^bDepartment of Bioengineering, Northeastern University, Boston, MA, 02115, USA

^cDepartment of Chemistry and Chemical Biology, Northeastern University, Boston, MA, 02115, USA

^dDepartment of Materials Science and Engineering, Drexel University, Philadelphia, PA, 19104, USA

† Electronic supplementary information (ESI) available. See DOI: <https://doi.org/10.1039/d4ra02678k>


determine whether these membranes are suitable for practical water desalination, the membranes require testing in pressure-driven mode.

Here, we have introduced two types of MXene composite membranes. (Type 1) $\text{Ti}_3\text{C}_2\text{T}_x + \text{WS}_2$ composite lamellar membrane, which has a van der Waals interaction between $\text{Ti}_3\text{C}_2\text{T}_x$ and WS_2 nanosheets. (Type 2) $\text{Ti}_3\text{C}_2\text{T}_x + \text{polymer}$ composite lamellar membrane where chemisorption of anionic polymer (polyvinyl phosphonic acid (PVPA)) on $\text{Ti}_3\text{C}_2\text{T}_x$ nanosheet surface takes place. For Type 1 membranes, mixing hydrophilic and flexible $\text{Ti}_3\text{C}_2\text{T}_x$ nanosheets with less hydrophilic and rigid WS_2 helps tune the surface properties, which is beneficial for water desalination. The composite membrane with a 2 : 1 mass ratio of $\text{Ti}_3\text{C}_2\text{T}_x$ and WS_2 allowed a more than 3-fold increase in water flux and almost the same salt rejection as the $\text{Ti}_3\text{C}_2\text{T}_x$ membrane. For Type 2 membranes, PVPA modification rendered the membrane highly negatively charged, improving salt rejection while maintaining a water permeance similar to the bare $\text{Ti}_3\text{C}_2\text{T}_x$ membrane. Hydrophilicity, and surface charge modulation help improve the membrane's performance.

2. Results

2.1. $\text{Ti}_3\text{C}_2\text{T}_x + \text{WS}_2$ composite membrane

Exfoliated $\text{Ti}_3\text{C}_2\text{T}_x$ sheets with dimensions ranging from 10–100 μm were sonicated (up to 1.5 hours) using a 100 W ultrasonic probe at 60% amplitude to obtain nanosheets. Fig. 1a and b show an AFM image of nanosheets before and after 1.5 hours of ultrasonic probe treatment, respectively. While before sonication, the sheets appear faceted and have straight edges, upon sonication, we observed nanosheets with a more rounded edge structure and a \sim 30-fold reduction in nanosheet size (Fig. S1a and b†). Likewise, WS_2 nanosheets obtained from the liquid phase exfoliation method (see Fig. 1c) exhibit a similar structure to $\text{Ti}_3\text{C}_2\text{T}_x$ nanosheets. We prepared $\text{Ti}_3\text{C}_2\text{T}_x$ membranes from different-sized nanosheets using the vacuum filtration method on 0.03 μm pore-sized poly (ether sulfone) (PES, see Methods) substrate as shown in Fig. 1d and measured X-ray diffraction (XRD) spectra. For the $\text{Ti}_3\text{C}_2\text{T}_x$ membrane made of unsonicated $\text{Ti}_3\text{C}_2\text{T}_x$ sheets, an intense 002 peak was observed at 6.7° with a full width at half maximum (FWHM) of 0.5° . A slight shift in the 002-peak position from 6.7° to 6.6° , but a significant reduction in peak intensity with a larger FWHM (1.0°) for the same mass per unit area of $\text{Ti}_3\text{C}_2\text{T}_x$ was observed after 1.5 hours of ultrasonic probe treatment (Fig. 1e). The reduced intensity and the broad XRD peak from the membrane prepared from sonicated nanosheets are due to a less regular lamellar structure. Based on the XRD patterns, the interlayer spacing in the $\text{Ti}_3\text{C}_2\text{T}_x$ membrane is 13.2–13.4 \AA . An interlayer void space of 3.4–3.6 \AA , obtained after subtracting the crystallographic monolayer thickness of $\text{Ti}_3\text{C}_2\text{T}_x$ (9.8 \AA),^{30–32} is minimal and may lead to slow water transport. To increase the void space, we prepared a composite membrane from a mixed dispersion of $\text{Ti}_3\text{C}_2\text{T}_x$ and WS_2 nanosheets in a 2 : 1 mass ratio using vacuum-assisted filtration. The XRD pattern of the composite membrane includes two peaks corresponding to $\text{Ti}_3\text{C}_2\text{T}_x$ at 6.2° with

a FWHM of 1.8° and to WS_2 at 14.3° with a FWHM of 0.7° but with reduced intensity (Fig. 1d, inset), which confirms that $\text{Ti}_3\text{C}_2\text{T}_x$ and WS_2 nanosheets are intermixed within the membrane. The mean water contact angles of $\text{Ti}_3\text{C}_2\text{T}_x$ (Fig. 1f) are slightly lower than for the composite membrane, revealing that the composite membrane is more hydrophobic than the $\text{Ti}_3\text{C}_2\text{T}_x$ membrane, possibly due to the contribution of the more hydrophobic WS_2 nanosheets. Slightly increased surface parameters, root mean square roughness (R_q , pixel) from 61 to 67 and average roughness (R_a , pixel) from 37 to 41, due to intermixing of different types of nanosheets were also observed (see Fig. S1d and e, and Table S1†). Based on the SEM cross-section image and EDX elemental mapping (Fig. S2a†), the presence of W and Ti throughout the membrane thickness further confirms the uniform distribution of $\text{Ti}_3\text{C}_2\text{T}_x$ and WS_2 nanosheets within the membrane. HAADF-STEM images, along with their EDX elemental maps (Fig. 1g, h, S2b–d†), show that multilayer $\text{Ti}_3\text{C}_2\text{T}_x$ and WS_2 stack within the membrane interchangeably and with a good degree of alignment. The SEM cross-section image (Fig. 1i) shows that the membrane is \sim 0.5 μm thick.

The composite membranes were tested in a cross-flow system,³³ as shown in Fig. 2a and S4.† First, a dispersion of $\text{Ti}_3\text{C}_2\text{T}_x$ in de-ionized (DI) water with a concentration of 0.2 mg mL^{-1} was sonicated using a 100 W ultrasonic probe at 60% amplitude for 30 min, and the membranes were prepared by varying the WS_2 and $\text{Ti}_3\text{C}_2\text{T}_x$ content in the membrane and tested for desalination against sodium sulphate salt. The water permeance of the $\text{Ti}_3\text{C}_2\text{T}_x$ membrane without WS_2 reported in this study is smaller than reported in the previous studies.^{25,28} In $\text{Ti}_3\text{C}_2\text{T}_x$ membranes, the water flow through the membrane depends on the distribution of surface terminations, which in turn depends on the nanosheet synthesis process. Here, $\text{Ti}_3\text{C}_2\text{T}_x$ nanosheets were synthesized using a method different (direct use of hydrofluoric acid)³⁴ from those used in previous studies. Furthermore, the applied pressure during filtration experiments was much higher (20 bar) than in the previous studies (\sim 1 bar). Based on an earlier study, applied pressure and electrostatic interactions between nanosheets are critical in controlling interlayer spacing. High-pressure compaction leads to the shrinkage of nanochannels, while electrostatic repulsion, resulting from negative surface charges, prevents the nanosheets from collapsing onto each other, thereby maintaining the interlayer spacing.³⁵ As the WS_2 mass ratio increases in the composite, water permeance through the membrane increases and salt rejection decreases (Fig. 2b); both changes are non-linear, possibly due to the impact of WS_2 on the degree of disorder within the lamellar membrane. We find for $\text{Ti}_3\text{C}_2\text{T}_x : \text{WS}_2$ that a 2 : 1 mass ratio is optimal.

$\text{Ti}_3\text{C}_2\text{T}_x$ nanosheets were sonicated for up to 1.5 hours, mixed with WS_2 nanosheets to prepare different membranes, and tested against $0.02 \text{ M Na}_2\text{SO}_4$ salt. The results are reported in Fig. 2c. We find that water permeance increases linearly with the sonication time of $\text{Ti}_3\text{C}_2\text{T}_x$ nanosheets while salt rejection is constant. Since the nanosheet size decreases with an increasing sonication time, the number of pathways for water within the membrane increases, consequently increasing the water



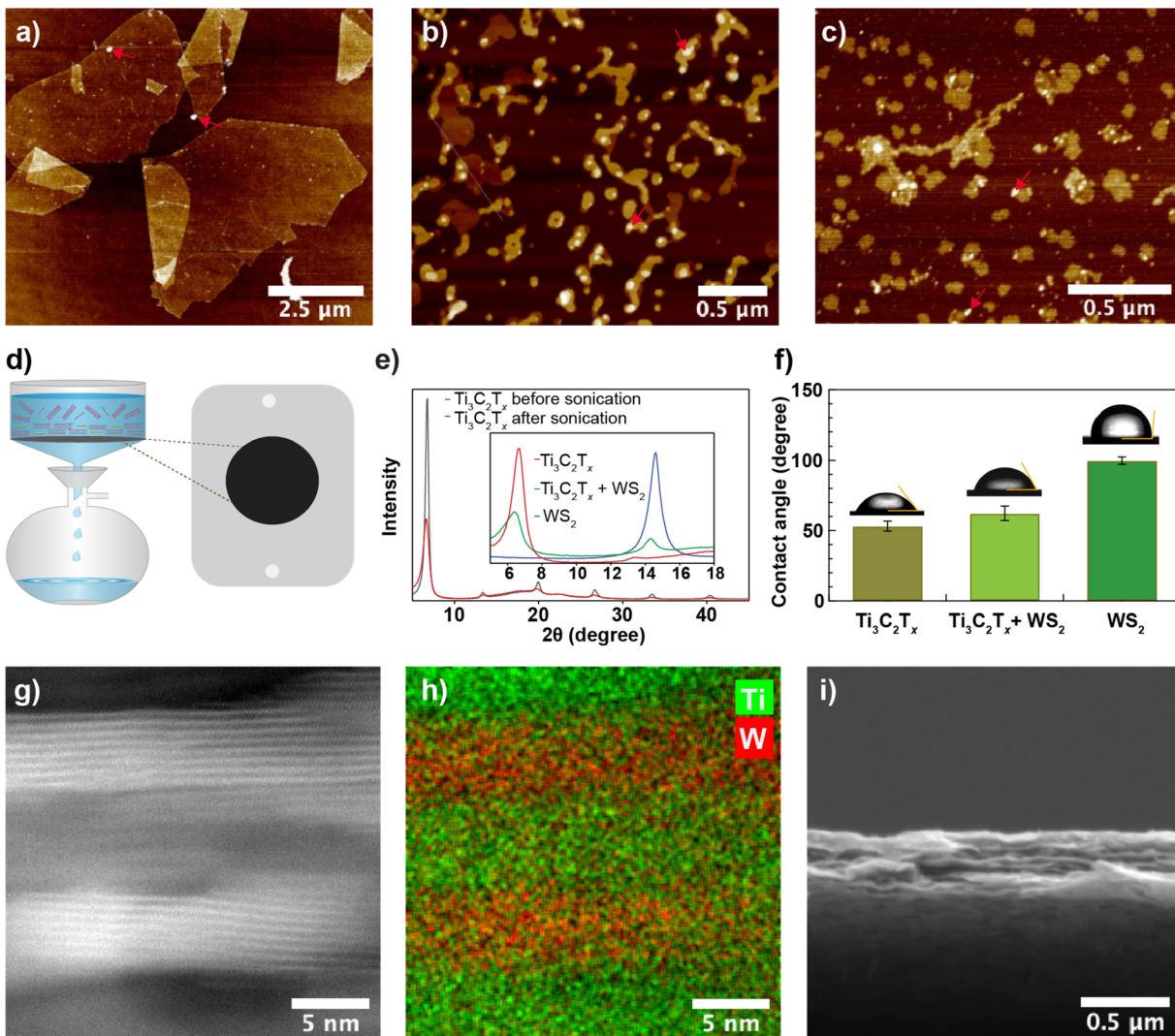


Fig. 1 Nanosheets and membrane characterization for $\text{Ti}_3\text{C}_2\text{T}_x + \text{WS}_2$ (2 : 1) composite membranes; (a–c) AFM images of $\text{Ti}_3\text{C}_2\text{T}_x$ nanosheets before (a) and after (b) 1.5 hours of ultrasonic probe treatment, as well as WS_2 nanosheets after sonication (c). Bright spots, shown by red arrows in (a), (b) and (c), might be residues. (d) Schematic showing vacuum filtration for membrane fabrication. (e) Comparison of XRD spectra before and after ultrasonic treatment; inset compares the XRD spectra of the $\text{Ti}_3\text{C}_2\text{T}_x$, WS_2 and $\text{Ti}_3\text{C}_2\text{T}_x + \text{WS}_2$ composite membrane ($\text{Ti}_3\text{C}_2\text{T}_x$ used in the inset was treated with ultrasonic probe for 1.5 hours). (f) Water contact angle comparison of $\text{Ti}_3\text{C}_2\text{T}_x$, $\text{Ti}_3\text{C}_2\text{T}_x + \text{WS}_2$, and WS_2 membrane (error bars represent the standard deviations of at least three measurements). (g and h) Cross section of $\text{Ti}_3\text{C}_2\text{T}_x + \text{WS}_2$ composite membrane; (g) HAADF-STEM image along with its false-color EDX elemental maps for Ti (green) and W (red) (h), and (i) side-view SEM image of the membrane. For all characterization, $\text{Ti}_3\text{C}_2\text{T}_x + \text{WS}_2$ composite membranes were prepared with 2 : 1 mass ratio of $\text{Ti}_3\text{C}_2\text{T}_x$ and WS_2 .

permeance. The mixed membrane with a mass ratio of 2 : 1 between $\text{Ti}_3\text{C}_2\text{T}_x$ (1.5 hours of probe-sonicated nanosheets) and WS_2 gives $\sim 90\%$ of Na_2SO_4 rejection (at 0.02 M Na_2SO_4 concentration) and $>0.6 \text{ Lm}^{-2} \text{ h}^{-1} \text{ bar}^{-1}$ of water permeance, 3 times higher than that of the $\text{Ti}_3\text{C}_2\text{T}_x$ membrane (made from 1.5 hours of sonicated nanosheets as shown in Fig. S5†). The observation of higher water permeance during the vacuum filtration of mixed nanosheets, as compared to $\text{Ti}_3\text{C}_2\text{T}_x$ nanosheets, indicates that the WS_2 nanosheets provide less resistance to water flow (shown in Fig. S3†). Previous studies have also reported higher water permeance through the WS_2 membrane³⁶ compared to the MXene membrane²⁵ for the same thickness. Thus, water permeance increases by increasing the

content of WS_2 nanosheets in the mixed membrane. The altered surface chemistry due to the mixing of two kinds of nanosheets, with a similar nanosheet size (shown in Fig. S1b and c†), a similar membrane thickness (shown in Fig. S9†) and a similar value of zeta potential around -60 mV (shown in Fig. S6†), maintains a higher Na_2SO_4 rejection. Different salt solutions were pressurized through the membrane at a pressure of 20 bar; the membrane rejected $>85\%$ of salts with a divalent anion and $>67\%$ of salts with a monovalent anion (shown in Fig. 2d and S7i†). The rejection of monovalent salt reported here is higher than that of most of the 2D-based lamellar membranes reported in the literature^{10,37,38} (shown in Fig. S11†) but lower than that of the TFC membrane.³⁹ The membrane's performance was stable

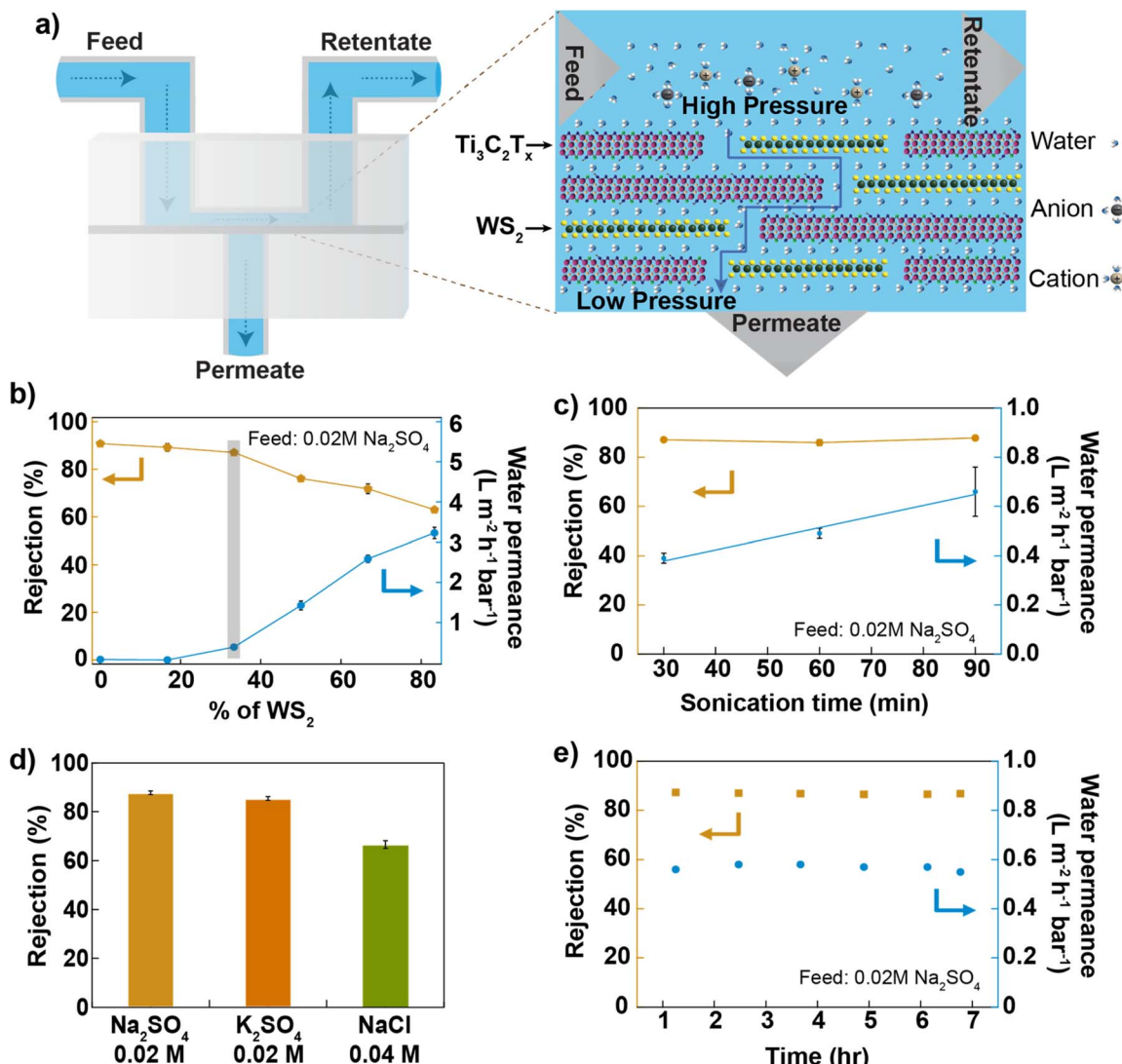


Fig. 2 Ti₃C₂T_x + WS₂ composite membrane's test in cross-flow systems; (a) Illustration of Ti₃C₂T_x + WS₂ composite membrane in the cross-flow cell. (b) Performance of Ti₃C₂T_x + WS₂ composite membrane based on WS₂ content, Ti₃C₂T_x was sonicated for 30 min. (c) Performance of Ti₃C₂T_x + WS₂ composite membrane by varying sonication time of Ti₃C₂T_x nanosheets. (d) Salt rejection of Ti₃C₂T_x + WS₂ composite membrane for different salts (each salt at 0.02 M concentration). (e) Stability test of Ti₃C₂T_x + WS₂ composite membrane for up to 7 hours. In each figure, error bars represent standard deviations from >3 replicates.

to within (2%) for up to 7 hours of tested time (Fig. 2e). The membrane was also tested for pressure-dependent performance, and the result is shown in Fig. S7ii.† The membrane maintained >67% NaCl rejection (at 0.04 M NaCl concentration) when tested up to 32 bar of applied.

2.2. Ti₃C₂T_x + PVPA composite membrane

Based on the XRD spectra of the Ti₃C₂T_x membrane, the interlayer void space of the dry membrane (3.3 to 3.5 Å) is minimal, due to which a small amount of water permeates through the membrane. To increase interlayer spacing by a minimal amount and alter the surface chemistry, we chose polyvinyl phosphonic acid (PVPA), an anionic polymer with a molecular weight of 24 000 Da and polydispersity of 1.24, as an intercalant.

The shift in the leftmost UV-vis absorbance peak from 268 nm to 274 nm (Fig. 3a) after introducing PVPA intercalant in

the suspension confirms the chemisorption of PVPA by Ti₃C₂T_x nanosheet. The bonding nature between PVPA and Ti₃C₂T_x nanosheets⁴⁰ may involve covalent and hydrogen bonding. Phosphorous of PVPA can interact with hydroxyl groups of Ti₃C₂T_x through a hetero-condensation reaction to form a P-O-Ti bond. In addition, functional groups of Ti₃C₂T_x, mainly =O and -OH, can form hydrogen bonding with -OH and =O groups coordinated to the phosphorous of PVPA. Fig. 3b compares the XRD spectra of Ti₃C₂T_x and Ti₃C₂T_x + PVPA composite membrane. The shift in the 002 XRD peak towards a smaller angle from 6.6° with a FWHM of 0.8° to 6.4° with a FWHM of 1.3° after PVPA functionalization shows that PVPA increases the interlayer void space from 3.6 Å to 4.0 Å. The zeta potentials of different dispersions were measured and compared in Fig. S6.† The change in zeta potential after PVPA modification is around -20 mV at pH 7, which makes the



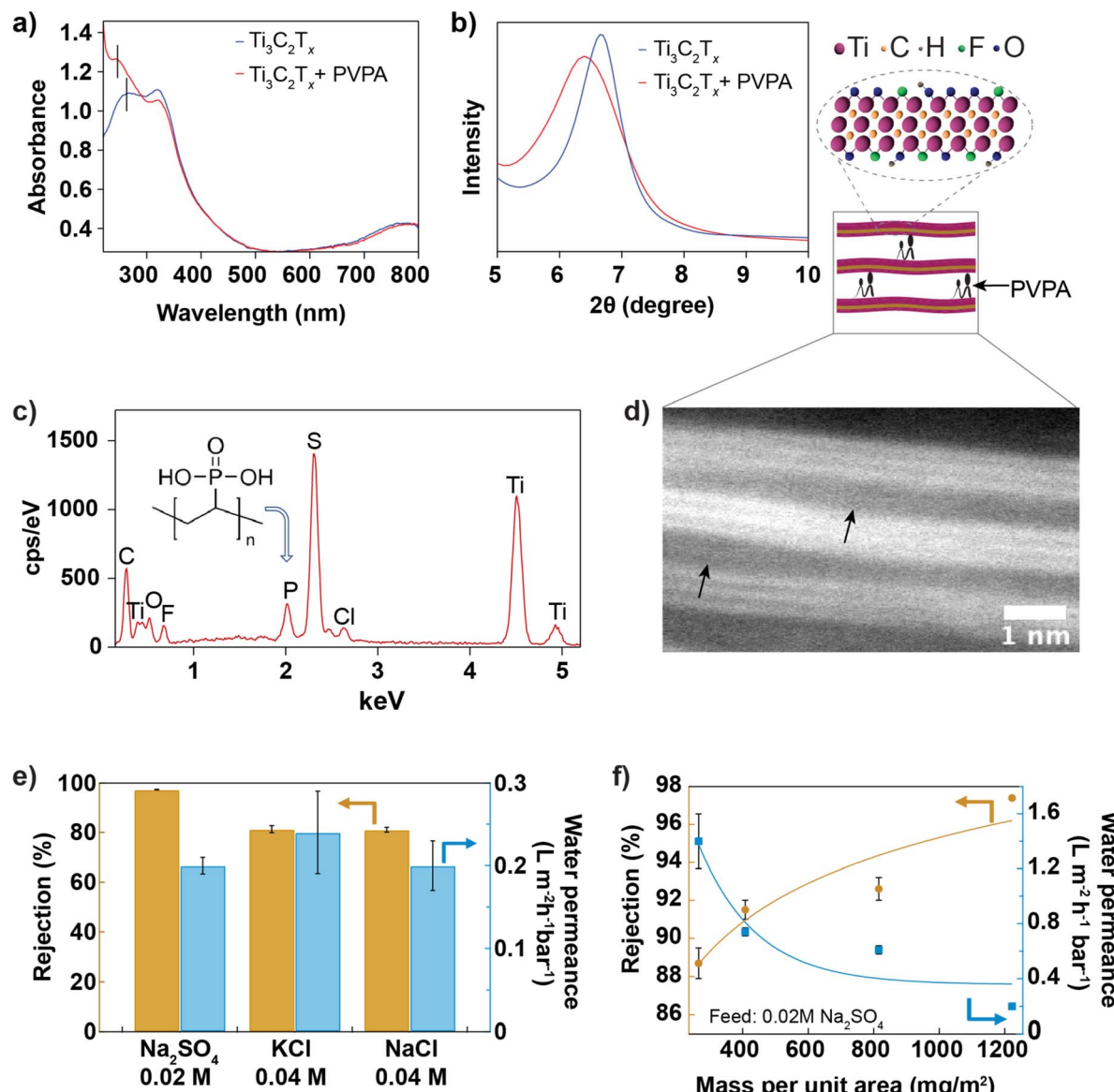


Fig. 3 Characterization and performance of $\text{Ti}_3\text{C}_2\text{T}_x + \text{PVPA}$ composite membrane. (a) Comparison of UV-vis spectra of $\text{Ti}_3\text{C}_2\text{T}_x + \text{PVPA}$ with that of $\text{Ti}_3\text{C}_2\text{T}_x$ dispersion. (b) XRD of different membranes. (c) EDX spectrum from the surface of the $\text{Ti}_3\text{C}_2\text{T}_x + \text{PVPA}$ composite membrane. (d) High-resolution TEM image of a cross-section of $\text{Ti}_3\text{C}_2\text{T}_x + \text{PVPA}$ composite membrane with arrows showing possible binding sites of PVPA with $\text{Ti}_3\text{C}_2\text{T}_x$ nanosheets and schematic illustration of the cross-section. (e) Salt rejection and water permeance of $\text{Ti}_3\text{C}_2\text{T}_x + \text{PVPA}$ composite membrane for different salts (concentration of Na_2SO_4 salt solution was 0.02 M and that of KCl was 0.04 M); error bars represent the standard deviations of three independent replicates. (f) Mass-dependent performance of the composite membrane; error bars represent the standard deviations of >3 replicates. Solid curves are provided to guide the eye.

composite membrane highly negatively charged. To further confirm the presence of PVPA within the membrane, we imaged the surface of the composite membrane using SEM and collected EDX data (see Fig. 3c). The presence of a phosphorous peak in the EDX spectrum confirms PVPA intercalation. The sulfur peak comes from the poly(ether-sulfone) substrate. The membrane's cross-section was $\sim 0.5 \mu\text{m}$ thick, confirmed with SEM, as shown in Fig. 3d and S9.† The inset shows a high-resolution TEM image of the composite membrane with the arrows pointing to the interlayer expanded regions; the interlayer expansion might have been caused by intercalated PVPA molecules.

For optimization, PVPA was mixed with $\text{Ti}_3\text{C}_2\text{T}_x$ dispersion, and the membranes were prepared under 3 different conditions: for type I membrane, the membrane was prepared by mixing 1% PVPA with 0.05 mg mL^{-1} of $\text{Ti}_3\text{C}_2\text{T}_x$ dispersion and drying at room temperature; for type II membrane, the membrane was prepared by mixing 1% PVPA with 0.05 mg mL^{-1} of $\text{Ti}_3\text{C}_2\text{T}_x$ dispersion and drying at 80°C for one day; for type III membrane, the dispersion (1% PVPA with 0.1 mg mL^{-1}) was heated at 80°C to 90°C for about 20 min, and the membrane was manufactured and dried at room temperature. In Fig. S8,† the performance of these three types of membranes was compared with the performance of the bare $\text{Ti}_3\text{C}_2\text{T}_x$

membrane. The performance of type III membranes was better than that of other membranes. MXene and PVPA composite dispersion was further optimized by heating 1% of PVPA with 0.2 mg mL⁻¹ of MXene at 80 °C to 90 °C for ~20 min to improve the binding between MXene and PVPA. According to previous studies, heat helps the hetero-condensation reaction by promoting P–O–Ti covalent bonding *via* hydrogen bonding interactions between P–OH and Ti–OH.^{40,41} The membrane prepared from this dispersion was referred to as $\text{Ti}_3\text{C}_2\text{T}_x$ + PVPA composite membrane. Fig. 3e shows the performance of the membrane against salts with monovalent and divalent anions. The rejection of sodium sulphate salt (0.02 M) is greater than 97%, while the rejection of potassium chloride (0.04 M) is ~80%. Salt rejection observed here is higher than that of the functionalized MoS_2 membranes,¹⁵ GO-based membranes,^{37,38,42} and MXene-based membranes²⁹ reported earlier (shown in Fig. S11†) but lower than that of the TFC membrane.³⁹ The high rejection for both salts is due to the synergistic effect of charge repulsion and size exclusion, as the membrane is highly negatively charged and possesses a small interlayer spacing. A previous study suggests that increasing salt rejection is more important than increasing water permeance for energy efficient desalination.⁴³ We have also investigated the rejection and permeance dependence on the mass of $\text{Ti}_3\text{C}_2\text{T}_x$ per unit area (while keeping PVPA at 1% by mass) and found that rejection increases with the mass per unit area, but permeance decreases, as shown in Fig. 3f. We also note that the $\text{Ti}_3\text{C}_2\text{T}_x$ membranes quickly delaminated from the substrate (both PES and AAO) when soaked in an aqueous solution, while PVPA functionalization improved the adhesion of the $\text{Ti}_3\text{C}_2\text{T}_x$ membrane to the PES substrate.

2.3. Comparison of performance of MXene-based composite membranes

Fig. 4a and b compare the performance of different $\text{Ti}_3\text{C}_2\text{T}_x$ -based membranes prepared in this study, all having a similar thickness (as evidenced by SEM cross-section images, see Fig. S9†), under brackish water (0.02 M Na_2SO_4 , 0.04 M NaCl) and seawater (0.5 M NaCl) conditions. Surface chemistry modulation by mixing $\text{Ti}_3\text{C}_2\text{T}_x$ and WS_2 with different hydrophilicity in a 2:1 mass ratio but similar surface charge and

nanosheet size helps to increase the water permeance while maintaining a similar salt rejection as a 100% $\text{Ti}_3\text{C}_2\text{T}_x$ membrane, whereas surface charge modulation with the help of anionic polyelectrolyte improves salt rejection while keeping similar water permeance as the $\text{Ti}_3\text{C}_2\text{T}_x$ membrane as shown in Fig. 4a. $\text{Ti}_3\text{C}_2\text{T}_x$ + PVPA membrane exhibits superior rejection of NaCl compared to $\text{Ti}_3\text{C}_2\text{T}_x$ + WS_2 (2:1) membrane in both brackish and seawater conditions (see Fig. 4b).

2.4. Chlorine resistance

Chlorination is an essential step in water purification and desalination processes to control microbes and other fouling agents in the water. The current water desalination industry heavily depends on polymeric membranes whose performance degrades when exposed to chlorine in solution. So, there should be three additional steps in addition to desalination to protect the membrane from chlorination. First, the water is chlorinated to kill microbes present in the feed water, and next, the water feed is dechlorinated before passing to the desalination chamber, and finally, desalinated water is chlorinated again before sending to the water distribution center; these additional steps make the desalination industry costly.⁴⁴ The double-chlorination step is necessary because the desalination membranes have poor chlorine tolerance. Here, we have compared the chlorine tolerance of $\text{Ti}_3\text{C}_2\text{T}_x$ + PVPA with that of Toray membranes with and without exposure to 4000 ppmh of NaOCl in cross-flow for 0.02 M Na_2SO_4 . We find that both salt and water permeation increase after bleach treatment through both types of membranes, while the relative level of degradation in the $\text{Ti}_3\text{C}_2\text{T}_x$ + PVPA membrane is much lower than for the Toray membrane. The increase in water flux after chlorine treatment is 24% through $\text{Ti}_3\text{C}_2\text{T}_x$ + PVPA membrane and 39% through Toray membrane (see Fig. 5). This result confirms that our $\text{Ti}_3\text{C}_2\text{T}_x$ + PVPA is ~62% more resistant to chlorine exposure than the commercial Toray membrane, with a slightly superior salt rejection. However, the Toray membrane still has a higher water permeance than our membranes. Further optimization of the 2D membrane layer (flake size, membrane thickness, porosity, chemical intercalants) may help to further increase the desalination performance of MXene-based membranes.

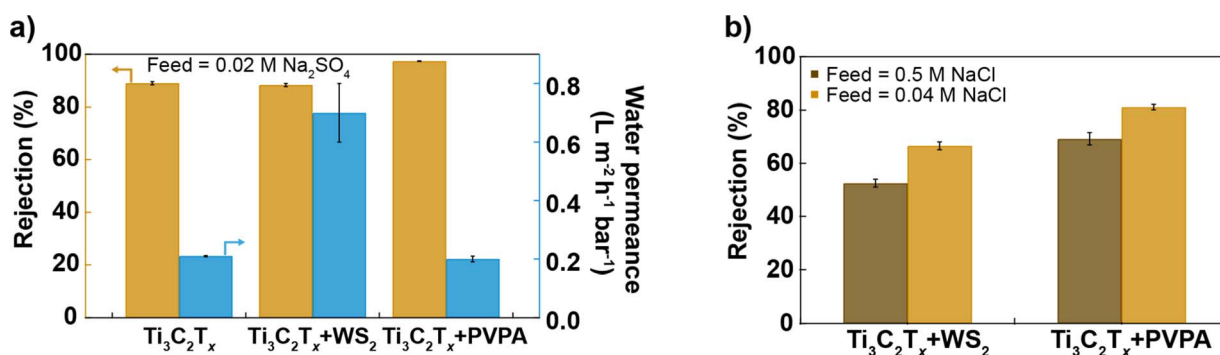


Fig. 4 Effect of hydrophilicity and surface charge modulation on the performance of MXene-based membranes. Comparison of performance of $\text{Ti}_3\text{C}_2\text{T}_x$ -based membranes in the cross-flow filtration system for 0.02 M Na_2SO_4 (a), and 0.04 M and 0.5 M NaCl (b). Error bars represent the standard deviations of at least three replicates.



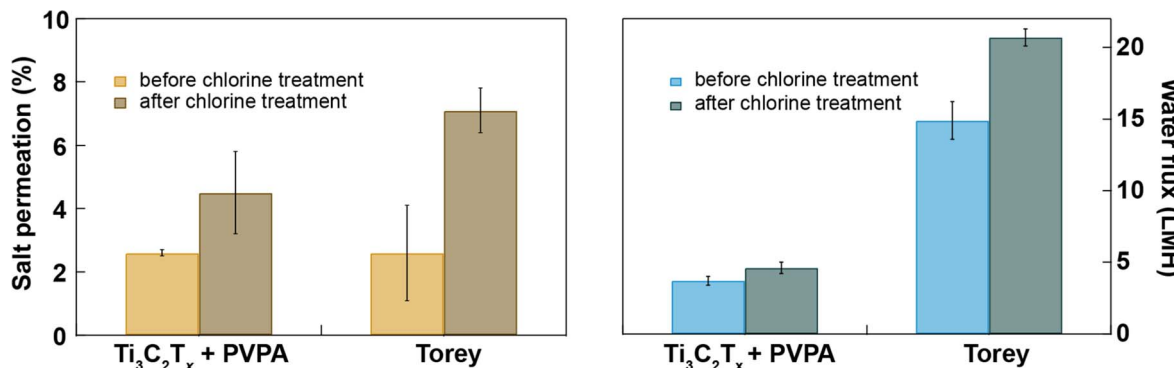


Fig. 5 Comparison of chlorine-resistance test of our $\text{Ti}_3\text{C}_2\text{T}_x$ + PVPA membranes Toray Flat sheet membranes, UTC-82V PA RO membrane (Sterlitech). Membranes (not treated with NaOCl solution and treated with 4000 ppmh of NaOCl solution) were tested in a cross-flow system with 0.02 M Na_2SO_4 as feed solution. Error bars represent the standard deviations of at least three replicates.

3. Conclusions

We have investigated $\text{Ti}_3\text{C}_2\text{T}_x$ -based membranes comprising surface-functionalized nanosheets for water desalination and found that an optimum balance between water permeance and salt rejection requires optimization of the preparation method and $\text{Ti}_3\text{C}_2\text{T}_x$ surface functionalization. Composite membranes that contain WS_2 added to the $\text{Ti}_3\text{C}_2\text{T}_x$ sheets offer improved water permeance without compromising salt rejection at optimal mass ratio of $\text{Ti}_3\text{C}_2\text{T}_x$ and WS_2 , presumably due to the more hydrophobic surface properties of WS_2 . On the other hand, hydrophilic polymer-based functionalization with the help of surface terminations present on the $\text{Ti}_3\text{C}_2\text{T}_x$ nanosheet surface helped improve salt rejection while maintaining water permeance similar to the $\text{Ti}_3\text{C}_2\text{T}_x$ membrane. Both membranes maintain high salt rejection when tested in the cross-flow pressurized system. However, there is still room for improvement in both salt rejection and water permeance of the membranes studied here compared to the commercial membrane. $\text{Ti}_3\text{C}_2\text{T}_x$ + PVPA membrane can also tolerate 4000 ppmh of chlorine (sodium hypochlorite) exposure significantly better than the commercially available Toray membrane, which confirms the applicability of $\text{Ti}_3\text{C}_2\text{T}_x$ -based membranes for water desalination. Given its low cost of manufacture, with further exploration of MXene membrane functionalization, we anticipate that MXene membranes for desalination/separation can reach commercialization in the coming years.

4. Methods and materials

4.1. 2D nanosheets synthesis and membrane fabrication

$\text{Ti}_3\text{C}_2\text{T}_x$ nanosheets were synthesized as described in a previous work.⁴⁵ The $\text{Ti}_3\text{C}_2\text{T}_x$ suspension was sonicated with the ultrasonic probe (Hielscher UP100H) at 60% amplitude for 30–90 min to reduce the size of nanosheets. The suspension was then centrifuged at 3500 rpm for 1 hour, and the supernatant was collected for further experiments. A well-established liquid phase exfoliation method⁴⁶ was utilized to obtain few-layered WS_2 nanosheets. In short, 1.5 g of bulk WS_2 powder (Sigma-Aldrich) with $\sim 2\ \mu\text{m}$ lateral-sized sheets was mixed with

100 mL of NMP (Fisher chemicals) solvent in a round bottom flask. The solution was treated with ultrasound in an ultrasonic bath (Branson 2510 Ultrasonic) for 5 hours and then in an ultrasonic probe for 3 hours to get desired-sized nanosheets. Then, the nanosheets were transferred from NMP to water. To remove the unexfoliated WS_2 sheets, the dispersion was centrifuged at 3000 rpm for 20 min. To eliminate unwanted chemicals, the suspension was dialyzed twice against 1 L of deionized water overnight.

$\text{Ti}_3\text{C}_2\text{T}_x$ and WS_2 were mixed in different mass ratios to fabricate various composite membranes. PES (0.03 μm pore-sized poly(ether sulfone), Sterlitech) was covered with an impermeable film, leaving a 2.5 cm diameter circular membrane area at the center. The mixed nanosheets were collected on a substrate using vacuum-assisted filtration with a mass loading of $1222\ \text{mg m}^{-2}$, unless otherwise mentioned. The membrane was left at room temperature overnight to dry. Quick-curing silicone elastomer (Ecoflex 5, Smooth-On) was applied to seal the gap between the deposited composite membrane and the impermeable membrane. The prepared membrane is shown in Fig. S4.† The optimized result was observed for the 2 : 1 mass ratio of MXene and WS_2 , so further experiments have proceeded with the same mass ratio.

The $\text{Ti}_3\text{C}_2\text{T}_x$ dispersions with concentrations of $0.05\ \text{mg mL}^{-1}$ to $0.2\ \text{mg mL}^{-1}$ were mixed with 0.5% to 1% of polyvinyl phosphonic acid PVPA. The optimized solution was prepared by mixing $0.02\ \text{mg mL}^{-1}$ of $\text{Ti}_3\text{C}_2\text{T}_x$ dispersion with 0.5% to 1% of PVPA, and the suspension was heated at 80–90 °C for 20 min to facilitate PVPA binding on $\text{Ti}_3\text{C}_2\text{T}_x$ nanosheets and cooled to room temperature and stored at 4 °C. The mixed solution was vacuum filtered to collect these modified nanosheets on the 0.03 μm pore-sized PES substrate.

4.2. Characterization

The nanosheets obtained after centrifugation were diluted in water, then deposited on a smooth silicon wafer and scanned using FastScan AFM (Bruker) using ScanAsyst air mode to see the size distribution of nanosheets in the dispersion. ImageJ was used to analyze the AFM images. X-ray diffraction (XRD) (Rigaku Ultima IV) with a $\text{Cu K}\alpha$ radiation source operating at 40



kV and 44 mA was used to observe the XRD patterns of the dry and wet membranes. Interlayer spacing was calculated using Bragg's law:

$$2d \sin(\theta) = n\lambda \quad (1)$$

where d is interlayer spacing, θ is the Bragg's angle which is the angle at the position of (002) peak, n is an integer representing diffraction series, and λ is the wavelength of the X-ray used.

The pH of the dispersion was adjusted to neutral by adding hydrochloric acid and potassium hydroxide drop by drop and continuously stirring the solution using a magnetic stirrer. The zeta potential and size distribution of different dispersions at neutral pH were measured using Zetasizer Nano ZS.

JEOL JSM-7000F was used for SEM and EDX. FEI Titan Themis 300 STEM in bright field mode was used for high-resolution TEM imaging.

Contact angles were measured using a homemade device, where images were recorded using a digital camera with Amscope software.

4.3. Membrane performance

For the filtration experiment, a CF016 cross-flow cell (Sterlitech) consisting of 39 mm long, 39 mm wide, and 2.3 mm deep rectangular channel was used. The membrane was fitted in the cross-flow cell and the feed tank was filled with the salt solution. The permeate was collected after the high-pressure pump (Hydra-cell pump, Wanner Engineering, Inc) pressurized the salt solution at 20 bar for brackish water and at 38 bar for sea water condition respectively through $\text{Ti}_3\text{C}_2\text{T}_x$, WS_2 and $\text{Ti}_3\text{C}_2\text{T}_x + \text{WS}_2$ membranes, and at 18 bar through the Toray Flat sheet membrane (UTC-82V PA RO membrane, Sterlitech). The active area of the Toray membrane was 20.6 cm^2 and that of MXene based membrane was $1.1\text{--}3.1 \text{ cm}^2$. The flow rate was 2 L min^{-1} for all experiments. Prior to beginning experiments, membranes were dried overnight in the air before starting desalination. Permeate flux was calculated with the following formula:

$$J = \frac{\Delta V}{At(\Delta P - \Delta \pi)} \quad (2)$$

where ΔV is permeated volume, A – effective membrane area, t – time required to collect a specific volume of permeate, and ΔP is the applied pressure and $\Delta \pi$ is osmotic pressure of the salt solution. To calculate salt rejection, the following formula was used:

$$R = 1 - \frac{C_p}{C_f} \quad (3)$$

where C_p is the concentration of salt in permeate and C_f is the concentration of salt in feed. First, the conductivities of feed and permeate were measured using a Mettler Toledo InLab 751-4mm Conductivity sensor, and the concentration of the salt solution was evaluated from the conductivity *vs.* concentration curve. The rejection value calculated from conductivity is the same as that calculated from concentration since concentration and conductivity are linearly related, as shown in Fig. S10.†

4.4. Chlorine resistance

Membranes were immersed in 4000 ppm of NaOCl for 1 h for the chlorine-resistance test. Then, membranes were tested in a cross-flow filtration system against 0.02 M Na_2SO_4 . Applied pressures were in the range of 18–20 bar.

Data availability

All data collected for this manuscript is available in <https://figshare.com/s/17fdb60939147b766379>.

Conflicts of interest

There are no conflicts to declare.

Acknowledgements

The authors are grateful to Dr Mehrnaz Mojtabavi for training on the use of MXenes in this work and for providing helpful suggestions. The authors thank Professor Sanjeev Mukerjee (Northeastern University) for the use of XRD for membrane characterization, Professor Ke Zhang (Northeastern University) for the use of the ZetaSizer Nano ZS for nanosheet characterization, and Dr Shirin Kaboli for her assistance with an experiment. The authors acknowledge the National Institutes of Health (R21HG011689) for funding this work.

References

- 1 A. Boretti and L. Rosa, *npj Clean Water*, 2019, **2**, 15.
- 2 R. Yang, Y. Fan, L. Mei, H. S. Shin, D. Voiry, Q. Lu, J. Li and Z. Zeng, *Nat. Synth.*, 2023, **2**, 101–118.
- 3 Q. Zhang, L. Mei, X. Cao, Y. Tang and Z. Zeng, *J. Mater. Chem. A*, 2020, **8**, 15417–15444.
- 4 C. E. Shuck, A. Sarycheva, M. Anayee, A. Levitt, Y. Zhu, S. Uzun, V. Balitskiy, V. Zahorodna, O. Gogotsi and Y. Gogotsi, *Adv. Eng. Mater.*, 2020, **22**, 1901241.
- 5 Y. Han, Z. Xu and C. Gao, *Adv. Funct. Mater.*, 2013, **23**, 3693–3700.
- 6 P. Sun, F. Zheng, M. Zhu, Z. Song, K. Wang, M. Zhong, D. Wu, R. B. Little, Z. Xu and H. Zhu, *ACS Nano*, 2014, **8**, 850–859.
- 7 R. R. Nair, H. A. Wu, P. N. Jayaram, I. V. Grigorieva and A. K. Geim, *Science*, 2012, **335**, 442–444.
- 8 C.-N. Yeh, K. Raidongia, J. Shao, Q.-H. Yang and J. Huang, *Nat. Chem.*, 2015, **7**, 166–170.
- 9 J. Abraham, K. S. Vasu, C. D. Williams, K. Gopinadhan, Y. Su, C. T. Cherian, J. Dix, E. Prestat, S. J. Haigh, I. V. Grigorieva, P. Carbone, A. K. Geim and R. R. Nair, *Nat. Nanotechnol.*, 2017, **12**, 546–550.
- 10 M. Hu and B. Mi, *Environ. Sci. Technol.*, 2013, **47**, 3715–3723.
- 11 H. Liu, H. Wang and X. Zhang, *Adv. Mater.*, 2015, **27**, 249–254.
- 12 K. Guan, S. Wang, Y. Ji, Y. Jia, L. Zhang, K. Ushio, Y. Lin, W. Jin and H. Matsuyama, *J. Mater. Chem. A*, 2020, **8**, 25880–25889.



13 E. Hoenig, S. E. Strong, M. Wang, J. M. Radhakrishnan, N. J. Zaluzec, J. L. Skinner and C. Liu, *Nano Lett.*, 2020, **20**, 7844–7851.

14 L. Ries, E. Petit, T. Michel, C. C. Diogo, C. Gervais, C. Salameh, M. Bechelany, S. Balme, P. Miele, N. Onofrio and D. Voiry, *Nat. Mater.*, 2019, **18**, 1112–1117.

15 W. Hirunpinyopas, E. Prestat, S. D. Worrall, S. J. Haigh, R. A. W. Dryfe and M. A. Bissett, *ACS Nano*, 2017, **11**, 11082–11090.

16 B. Sapkota, W. Liang, A. VahidMohammadi, R. Karnik, A. Noy and M. Wanunu, *Nat. Commun.*, 2020, **11**, 2747.

17 Z. Wang, Q. Tu, S. Zheng, J. J. Urban, S. Li and B. Mi, *Nano Lett.*, 2017, **17**, 7289–7298.

18 B. Anasori, M. R. Lukatskaya and Y. Gogotsi, *Nat. Rev. Mater.*, 2017, **2**, 16098.

19 M. R. Lukatskaya, S. Kota, Z. Lin, M.-Q. Zhao, N. Shpigel, M. D. Levi, J. Halim, P.-L. Taberna, M. W. Barsoum, P. Simon and Y. Gogotsi, *Nat. Energy*, 2017, **2**, 17105.

20 A. VahidMohammadi, A. Hadjikhani, S. Shahbazmohamadi and M. Beidaghi, *ACS Nano*, 2017, **11**, 11135–11144.

21 Z. W. Seh, K. D. Fredrickson, B. Anasori, J. Kibsgaard, A. L. Strickler, M. R. Lukatskaya, Y. Gogotsi, T. F. Jaramillo and A. Vojvodic, *ACS Energy Lett.*, 2016, **1**, 589–594.

22 M. Mojtabavi, A. VahidMohammadi, W. Liang, M. Beidaghi and M. Wanunu, *ACS Nano*, 2019, **13**, 3042–3053.

23 Z. Lu, Y. Wei, J. Deng, L. Ding, Z.-K. Li and H. Wang, *ACS Nano*, 2019, **13**, 10535–10544.

24 L. Ding, L. Li, Y. Liu, Y. Wu, Z. Lu, J. Deng, Y. Wei, J. Caro and H. Wang, *Nat. Sustainability*, 2020, **3**, 296–302.

25 C. E. Ren, K. B. Hatzell, M. Alhabeb, Z. Ling, K. A. Mahmoud and Y. Gogotsi, *J. Phys. Chem. Lett.*, 2015, **6**, 4026–4031.

26 C. E. Ren, M. Alhabeb, B. W. Byles, M.-Q. Zhao, B. Anasori, E. Pomerantseva, K. A. Mahmoud and Y. Gogotsi, *ACS Appl. Nano Mater.*, 2018, **1**, 3644–3652.

27 M. Naguib, M. Kurtoglu, V. Presser, J. Lu, J. Niu, M. Heon, L. Hultman, Y. Gogotsi and M. W. Barsoum, *Adv. Mater.*, 2011, **23**, 4248–4253.

28 G. Zeng, Q. Lin, K. Wei, Y. Liu, S. Zheng, Y. Zhan, S. He, T. Patra and Y.-H. Chiao, *J. Mater. Sci.*, 2021, **56**, 6814–6829.

29 J. Zhu, L. Wang, J. Wang, F. Wang, M. Tian, S. Zheng, N. Shao, L. Wang and M. He, *ACS Nano*, 2020, **14**, 15306–15316.

30 J. Halim, M. R. Lukatskaya, K. M. Cook, J. Lu, C. R. Smith, L.-Å. Näslund, S. J. May, L. Hultman, Y. Gogotsi, P. Eklund and M. W. Barsoum, *Chem. Mater.*, 2014, **26**, 2374–2381.

31 X. Wang, X. Shen, Y. Gao, Z. Wang, R. Yu and L. Chen, *J. Am. Chem. Soc.*, 2015, **137**, 2715–2721.

32 A. Lipatov, M. Alhabeb, M. R. Lukatskaya, A. Boson, Y. Gogotsi and A. Sinitskii, *Adv. Electron. Mater.*, 2016, **2**, 1600255.

33 W. Koros, Y. Ma and T. Shimidzu, *Pure Appl. Chem.*, 1996, **68**, 1479–1489.

34 T. S. Mathis, K. Maleski, A. Goad, A. Sarycheva, M. Anayee, A. C. Foucher, K. Hantanasisirakul, C. E. Shuck, E. A. Stach and Y. Gogotsi, *ACS Nano*, 2021, **15**, 6420–6429.

35 H. Huang, Y. Mao, Y. Ying, Y. Liu, L. Sun and X. Peng, *Chem. Commun.*, 2013, **49**, 5963–5965.

36 L. Sun, Y. Ying, H. Huang, Z. Song, Y. Mao, Z. Xu and X. Peng, *ACS Nano*, 2014, **8**, 6304–6311.

37 Q. Yang, Y. Su, C. Chi, C. T. Cherian, K. Huang, V. G. Kravets, F. C. Wang, J. C. Zhang, A. Pratt, A. N. Grigorenko, F. Guinea, A. K. Geim and R. R. Nair, *Nat. Mater.*, 2017, **16**, 1198–1202.

38 Y. Han, Y. Jiang and C. Gao, *ACS Appl. Mater. Interfaces*, 2015, **7**, 8147–8155.

39 M. Kadhom and B. Deng, *J. Water Proc. Engineering*, 2019, **30**, 100542.

40 P. J. Hotchkiss, S. C. Jones, S. A. Paniagua, A. Sharma, B. Kippelen, N. R. Armstrong and S. R. Marder, *Acc. Chem. Res.*, 2012, **45**, 337–346.

41 G. Guerrero, P. H. Mutin and A. Vioux, *Chem. Mater.*, 2001, **13**, 4367–4373.

42 A. Akbari, P. Sheath, S. T. Martin, D. B. Shinde, M. Shaibani, P. C. Banerjee, R. Tkacz, D. Bhattacharyya and M. Majumder, *Nat. Commun.*, 2016, **7**, 10891.

43 J. R. Werber, A. Deshmukh and M. Elimelech, *Environ. Sci. Technol. Lett.*, 2016, **3**, 112–120.

44 J. M. Gohil and A. K. Suresh, *J. Membr. Sci.*, 2017, **541**, 108–126.

45 M. Mojtabavi, W.-Y. Tsai, A. VahidMohammadi, T. Zhang, Y. Gogotsi, N. Balke and M. Wanunu, *Small*, 2022, **18**, 2105857.

46 J. N. Coleman, M. Lotya, A. O'Neill, S. D. Bergin, P. J. King, U. Khan, K. Young, A. Gaucher, S. De, R. J. Smith, I. V. Shvets, S. K. Arora, G. Stanton, H.-Y. Kim, K. Lee, G. T. Kim, G. S. Duesberg, T. Hallam, J. J. Boland, J. J. Wang, J. F. Donegan, J. C. Grunlan, G. Moriarty, A. Shmeliov, R. J. Nicholls, J. M. Perkins, E. M. Grieveson, K. Theuwissen, D. W. McComb, P. D. Nellist and V. Nicolosi, *Science*, 2011, **331**, 568.

